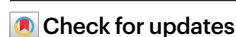


# Cation replacement method enables high-performance electrolytes for multivalent metal batteries

Received: 21 February 2023

Accepted: 11 December 2023

Published online: 8 January 2024



Siyuan Li<sup>1,4</sup>, Jiahui Zhang<sup>1,2,4</sup>, Shichao Zhang<sup>1,4</sup>, Qilei Liu<sup>3</sup>, Hao Cheng<sup>1,2</sup>, Lei Fan<sup>1</sup>, Weidong Zhang<sup>1</sup>, Xinyang Wang<sup>1</sup>, Qian Wu<sup>1,2</sup> & Yingying Lu<sup>1,2</sup>✉

High-performance, cost-efficient electrolyte systems are sought after for high-energy-density multivalent metal batteries. However, the expensive precursor and complex synthesis process hinders exploration of cathode electrode/electrolyte interfaces and solvation structures. Here we developed a universal cation replacement method to prepare low-cost, high-reversibility magnesium and calcium electrolytes derived from a zinc organoborate solvation structure. By rationally adjusting the precursor chain length and F-substitution degree, we can fine tune anion participation in the primary solvation shell. A completely dissociated Mg organoborate electrolyte enables high current endurance and enhanced electrochemical kinetics, whereas the Ca organoborate electrolyte with strong coordination/B–H inclusion offers a stable solid–electrolyte interphase with high coulombic efficiency. A rechargeable 53.4 Wh kg<sup>−1</sup> Mg metal prototype is achieved with a 30 μm Mg anode, a low electrolyte/sulfur ratio (E/S = 5.58 μl mg<sup>−1</sup>) and a modified separator/interlayer. This work provides innovative strategies for reversible electrolyte systems and high-energy-density multivalent metal batteries.

The growing electric vehicle market and the expanding electrochemical energy storage industry are in pursuit of advanced battery technologies with high-energy, high-safety and non-scarcity properties<sup>1–3</sup>. Among the next-generation post-lithium-ion battery chemistries, rechargeable divalent metal batteries with low-reduction-potential anodes, such as magnesium and calcium metal, have received widespread attention<sup>4–8</sup>. The considerable redox potential (−2.38 V versus standard hydrogen electrode for Mg and −2.76 V for Ca) offers enough voltage headroom to match high-voltage cathodes to fabricate a high-energy-density cell. The two-electron-transfer chemistry provides a higher volumetric energy density (3,832 mA h cm<sup>−3</sup> for Mg and 2,052.6 mA h cm<sup>−3</sup> for Ca) and high element abundance makes the raw materials low cost and available<sup>9,10</sup>.

Contrary to the use of cost-efficient anode materials, the development of a high-performance Mg/Ca single salt with high purity and scalable properties has gradually become the Achilles' heel for rechargeable Mg/Ca batteries<sup>11,12</sup>. In the first-generation Mg electrolyte, chloride and borohydride were proven to be good auxiliary anions to suppress the decomposition of the salt/solvent so that 99% reversible Mg electrodeposition could be achieved<sup>13–19</sup>. However, the low anodic stability and corrosive property exclude Cl<sup>−</sup>/BH<sub>4</sub><sup>−</sup>-containing electrolytes from industrial applications<sup>20,21</sup>. Therefore, non-corrosive chloride-free single-salt electrolyte systems are attracting intensive research, including fluoroalkoxy borates/aluminates (Mg(CB<sub>11</sub>H<sub>12</sub>)<sub>2</sub>, Mg(B(hfip)<sub>4</sub>)<sub>2</sub>, LiB(hfip)<sub>4</sub> and so on) and their derivative Ca(B(hfip)<sub>4</sub>)<sub>2</sub> (refs. 22–28). Although satisfactory reversibility (>95% for Mg and ~80%

<sup>1</sup>State Key Laboratory of Chemical Engineering, Institute of Pharmaceutical Engineering, College of Chemical and Biological Engineering, Zhejiang University, Hangzhou, China. <sup>2</sup>ZJU-Hangzhou Global Scientific and Technological Innovation Center, Hangzhou, China. <sup>3</sup>State Key Laboratory of Fine Chemicals, Frontiers Science Center for Smart Materials Oriented Chemical Engineering, Institute of Chemical Process Systems Engineering, School of Chemical Engineering, Dalian University of Technology, Dalian, China. <sup>4</sup>These authors contributed equally to this work: Siyuan Li, Jiahui Zhang, Shichao Zhang. ✉e-mail: [yingyinglu@zju.edu.cn](mailto:yingyinglu@zju.edu.cn)

for Ca) can be obtained, these weakly coordinating electrolyte systems with electron-delocalizing anions usually involve rare raw materials and complex synthesis steps<sup>29</sup>. For example,  $\text{Mg}(\text{BH}_4)_2/\text{Ca}(\text{BH}_4)_2$ , the precursor of magnesium/calcium organoborates, shows an ultrahigh price and a low purity (95%) due to its harsh synthetic environment, which will probably passivate the Mg/Ca surface and hinder further large-scale commercialization<sup>8,22,24</sup>. Methoxyethyl-amine chelants can improve the reversibility of magnesium and calcium, but the impact of  $-\text{NH}_2$  on the cycling performance needs to be investigated<sup>7</sup>. To date, developing a cost-effective synthetic route for impurity-free Mg/Ca salts is still a problem that has plagued the development of Mg/Ca-based batteries.

In this paper, we proposed a universal cation replacement method to prepare low-cost, high-performance magnesium and calcium electrolytes. First, the cost-effective and readily available  $\text{Zn}(\text{BH}_4)_2$  precursor was reacted with different fluoroalcohols to generate the target anions with varied branched chains. Then the  $\text{Zn}^{2+}$ -anion solvates were reacted with cheap metal foils with higher metal activity (for example, Ca, Mg) in ether conditions, resulting in the desired solvation structure (Fig. 1a). Specifically, the as-obtained anions with high F substitution and steric hindrance leaned towards a highly dissociative solvation shell, which was beneficial for improvements in ionic conductivity and high current endurance magnesium metal cells ( $25 \text{ mA cm}^{-2}$ ). Meanwhile, two types of Ca solvate, one with strong cation–anion coordination and the other B–H containing organoborate, offered  $\text{CaO}/\text{CaH}_x$ -based passivation layer with high Ca reversibility, suppressing continuous solvent decomposition and maintaining stable cycling. With these efforts, a high-loading Mg/S battery prototype with  $53.4 \text{ Wh kg}^{-1}$  was achieved by using a thin Mg anode, a lean Mg organoborate electrolyte, a thin poly(vinyl alcohol) (PVA) separator and a graphene oxide (GO)/Cu interlayer at  $60^\circ\text{C}$ .

## Synthesis and characterization of Ca and Mg solvates

The precursors used in currently available synthetic routes always have low purity and high prices (Supplementary Fig. 1), which leads to low metal reversibility and poor practicality. Meanwhile, several of these precursors have been hard to obtain from manufacturers since 2021 in Asia (for example,  $\text{Mg}(\text{BH}_4)_2$ ). The synthesis of borohydride usually starts from sodium borohydride and the corresponding chloride. Magnesium chloride/calcium chloride has difficulty dissolving in ether to form a complex<sup>30</sup>. Therefore, it is often prepared by solid-phase reaction (ball milling), resulting in low-purity borohydride, whereas zinc chloride can form a complex with ether/amine to obtain high-purity zinc borohydride through liquid-phase reaction<sup>29,31–33</sup>. Until now, the bill of materials (BOM) cost for mainstream high-performance weakly coordinating Mg electrolytes has been extremely high for  $\text{Mg}(\text{BH}_4)_2$ -derived (route 1), di-*n*-butylmagnesium-derived (route 2)  $\text{Mg}(\text{B}(\text{hfip})_4)_2$  and  $(\text{HNEt}_3)\text{CB}_{11}\text{H}_{12}$ -derived  $\text{Mg}(\text{CB}_{11}\text{H}_{12})_2$  (route 3) (Fig. 1b and Supplementary Fig. 2). Here we start from structurally similar and inexpensive  $\text{Zn}(\text{BH}_4)_2$ /tetrahydrofuran (THF) precursors and alcohols containing different fluorine contents to synthesize a series of Mg/Ca organoborates, which can reduce the BOM to the same order of magnitude as that for the state-of-the-art lithium-ion batteries currently available ( $92.96$  vs  $\text{US\$}14.93 \text{ kWh}^{-1}$ ). The proposed electrolytes are denoted  $\text{M}_x/\text{C}_x$  ( $x = 0, 1, 2, 3, 4, 5$ ) in 1,2-dimethoxyethane (DME) in which the anions of the 0 to 5 solvates have different  $-\text{CF}_3$  substitutions (Fig. 1c).

The detailed synthesis procedure and potential industrial amplification process are shown in Supplementary Figs. 3 and 4. Taking M2/C2 as examples,  $\text{Zn}(\text{BH}_4)_2$  first reacted with equal stoichiometric alcohol in a THF/DME solution to form the  $\text{Zn}^{2+}$  solvation sheath with the target anion (Supplementary Fig. 5) after which metallic Ca/Mg foils were placed in solution to form the target cation solvation sheath until a surface without any black Zn appeared. After purification and crystallization to remove  $\text{BH}_4^-$ , a 75 g M2 solvate was obtained with a

high yield of 92% (Fig. 1d). The obtained single crystal reveals that the target anion  $\text{B}(\text{hfip})_4^-$  is successfully prepared, in which  $\text{Mg}^{2+}$  chelates with three DME molecules and  $\text{Ca}^{2+}$  chelates with four DME molecules (Fig. 1e and Supplementary Fig. 6). Nuclear magnetic resonance (NMR) spectroscopy and electrospray ionization-mass spectrometry (ESI-MS) were carried out to examine the final solvation structure.  $^{19}\text{F}$  and  $^{11}\text{B}$  show only a single strong peak at  $-74.35 \text{ ppm}$  and  $1.56 \text{ ppm}$ , which proves that there is almost no impurity in the final target anion (Fig. 1f and Supplementary Fig. 7). The ESI-MS positive mode result shows a series of peaks with an  $m/z$  ratio at 102 and 147, corresponding to the  $(\text{Mg}(\text{DME})_2)_2^{2+}$  and  $(\text{Mg}(\text{DME})_3)_2^{2+}$  molecules, indicating that the anion does not participate in the cation solvation structure (Fig. 1g). The negative mode results only show a strong peak at 678.9823, indicating that solvated cation replacement does not destroy the anion (Fig. 1h). Inductively coupled plasma-mass spectrometry (ICP-MS) results show that the cations in the salt are the desired Mg (99.76%) and Ca (99.25%) cations (Fig. 1i).

Through this feasible cation replacement method, we further synthesized another five Ca/Mg anions to explore the effect of different branched chains on the metal deposition behaviour, including  $\text{B}(\text{Et})_4^-$ ,  $\text{B}(\text{tfe})_4^-$ ,  $\text{B}(\text{tf1p})_4^-$ ,  $\text{B}(\text{tf2p})_4^-$  and  $\text{BH}(\text{pftb})_3^-$ . The corresponding  $^{19}\text{F}$ ,  $^{11}\text{B}$  and  $^1\text{H}$  spectra also prove that these anions are successfully prepared (Supplementary Figs. 8–12). Among them, the M3/C3 anions are very different from the other tetrasubstituted organoborates (Fig. 1j). Due to the steric hindrance effect, the last branched hydrogen atom in the borohydride seems to be unable to react with perfluoro-tert-butanol, showing a triple-substitution characterization in ESI-MS, which is different from the previous report<sup>26</sup>. The ICP-MS tests also demonstrate satisfactory replacement of  $\text{Zn}^{2+}$  with  $\text{Mg}^{2+}$  or  $\text{Ca}^{2+}$  (Supplementary Fig. 13). The ionic conductivity of the various electrolytes under different concentrations is shown in Fig. 1k and Supplementary Fig. 14. Considering the maximum conductivity and solubility of various electrolytes, we chose 0.5 M for further electrochemical property tests.

## Solvation shell analysis

Theoretical simulation of six different anions was performed to detect the impact of the branched chain on the solvation shell (Fig. 2a). Density functional theory (DFT)-calculated electrostatic potential (ESP) maps of various anions show that the negative charge is mainly localized at the oxygen and boron atoms. With an increase in the fluorine substitution on the branched chain, the negative charge at the O atom is effectively dispersed (Fig. 2b), implying a reduced potential to coordinate with cations and a low possibility of participating in the solvation structure. The optimized binding configurations also give intuitive interactions of one cation with different anions (Supplementary Figs. 15 and 16) in which anions 0 and 1 offer the shortest cation–O distance ( $0 < 1 < 4 < 5 < 2 < 3$ ). As a result, the binding energies between one  $\text{Mg}^{2+}/\text{Ca}^{2+}$  ion and one anion (0 to 5) follow the same trend (Supplementary Fig. 17).

Molecular dynamics (MD) simulations were further performed to identify the solvation shell in different electrolytes under 0.5 M conditions (Fig. 2c). For anions 0 and 1, weak Mg–O (DME) and strong Mg–O (anion,  $2.18 \text{ \AA}$ ) and Mg–B ( $2.96 \text{ \AA}$ ) radial distribution functions can be observed (Supplementary Figs. 18 and 19), indicating the existence of close-contact ion pairs rather than cation–solvent (DME) interactions in the primary solvation shell. For anions 2 and 3, where the Mg–O (anion) and Mg–B peaks almost disappear and are replaced by an intense Mg–O (DME,  $2.26 \text{ \AA}$ ) peak. This result proves that the solvates are completely dissociated by the solvent without close-contact ion pairs. For anions 4 and 5 with moderate F substitution, both anions and DME participate in the solvation structure. Therefore, we can divide the solvation structure into three categories: close-contact solvation structure (anions 0 and 1), completely dissociated solvation structure (anions 2 and 3) and partially dissociated solvation structure (anions 4 and 5). Raman spectra obtained from Ca electrolytes prove the strong coordination between cations (C2 and C3) and DME at  $\sim 870 \text{ cm}^{-1}$ , which

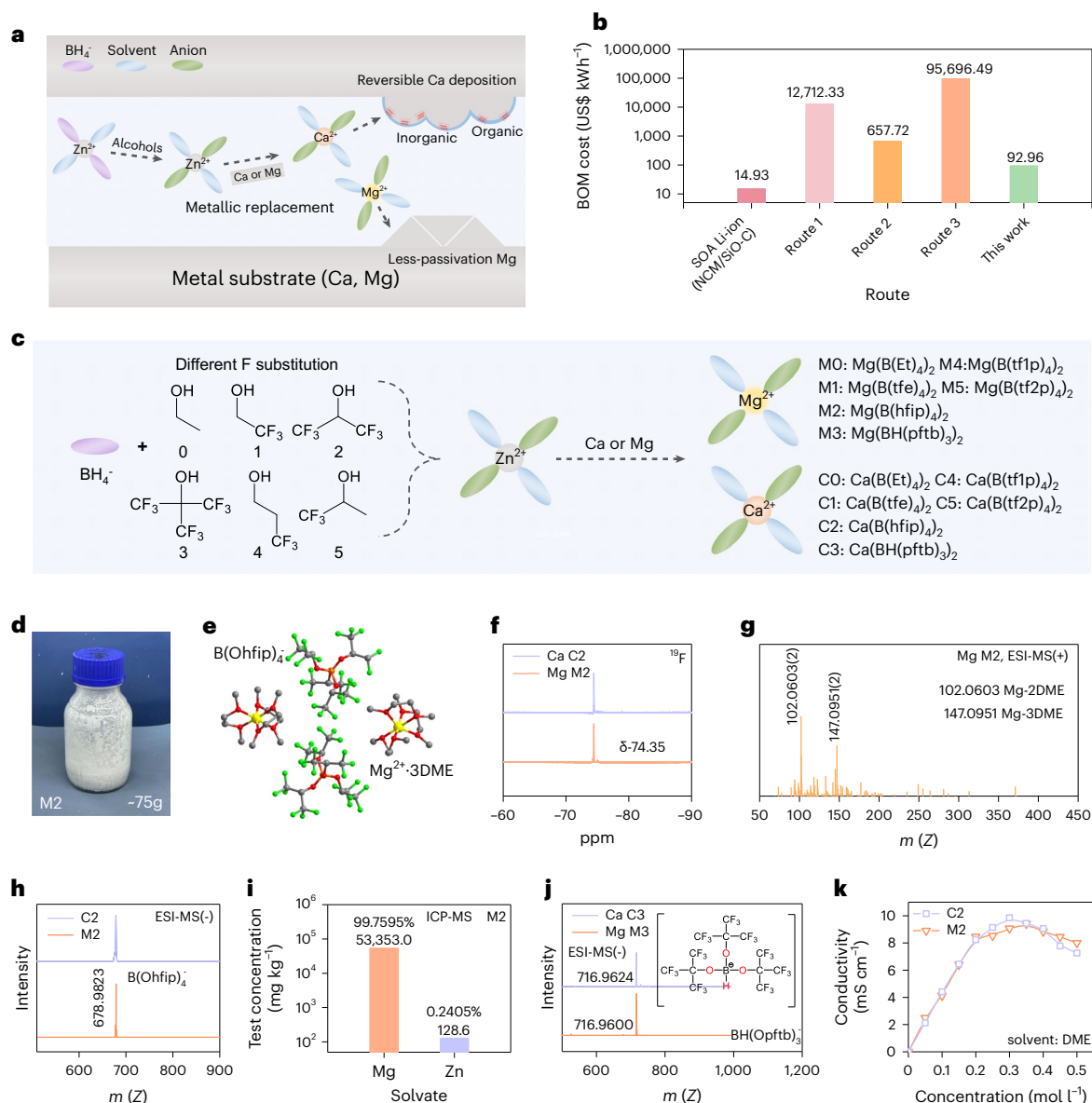


**Fig. 1 | Synthesis route and characterization of different Ca/Mg solvates.**

**a**, Schematic of the cation replacement method using a zinc organoborate solvation precursor: the Zn organoborate is first synthesized by reaction between  $\text{Zn}(\text{BH}_4)_2$  and alcohols, after which the  $\text{Zn}^{2+}$  is replaced by higher active Ca or Mg metal to obtain Ca/Mg solvates. Colour scheme of electrolyte components:  $\text{BH}_4^-$ , purple oval; solvent, blue oval; target anion, green oval. **b**, BOM costs of different routes for calcium and magnesium solvates and a commercial lithium-ion battery electrolyte (based on the price of 2023/03). **c**, Synthesis of corresponding magnesium/calcium solvates using various

precursors. **d**, Large-scale preparation of the M2 solvate in a 250 ml bottle.

**e**, DME-solvated M2 solvate obtained from X-ray single-crystal structure. Colour scheme of molecules: Mg, yellow; F, green; O, red; C, grey; B, orange. **f**,  $^{19}\text{F}$ -NMR spectra of C2/M2 in DMSO-d<sub>6</sub>. **g**, ESI-MS spectra of the M2 electrolyte (positive mode). **h**, ESI-MS spectra of the C2/M2 electrolytes (negative mode). **i**, ICP-MS results of the synthesized M2 solvate. **j**, ESI-MS spectra of the C3/M3 electrolytes (negative mode). **k**, Ionic conductivity dependence on the concentration of M2/C2 electrolytes at 30 °C.

is in accordance with the completely dissociated property (Supplementary Fig. 20).

Detailed information on the three solvation structures is described based on the distribution of  $\text{Mg}^{2+}$  solvates, which includes four types (Fig. 2d and Supplementary Fig. 21): solvent-surrounded metal ion<sup>2+</sup> ( $\text{SSM}^{2+}$ ,  $\text{Mg}^{2+}$ -anion<sup>-</sup>), partial contact ion pair ( $\text{pCIP}^+$ ,  $\text{Mg}^{2+}$ -anion<sup>-</sup>), full contact ion pair ( $\text{fCIP}$ ,  $\text{Mg}^{2+}$ -anion<sup>-</sup>) and metal ion<sup>2+</sup>-anion cluster ( $\text{MAC}^-$ ,  $\text{Mg}^{2+}$ -anion<sup>-</sup>). The close-contact solvation structure possesses many anions combined with cations ( $\text{MAC}^-$ ,  $\text{fCIP}$ ), indicating a lower dissociation degree and an anion-derived passivation layer. In contrast, the completely dissociated solvation structure shows a high dissociation degree with more mobile  $\text{Mg}^{2+}$ / $\text{Ca}^{2+}$  charge carriers

( $\text{SSM}^{2+}$  and  $\text{pCIP}^+$ ) that are responsible for a high ionic conductivity, which is also conducive to a low overpotential in symmetric cells. This trend agrees well with the ionic conductivity of the six electrolytes with minor deviations. This calculation conclusion also applies to the calcium homologues and obtains the same trend as the Mg solvation shell (Supplementary Fig. 22).

### Ca and Mg reversibility and passivation analysis

As shown in Fig. 3a, the Ca coulombic efficiency (CE) was evaluated using the Ca/Cu half cell under 2 mA cm<sup>-2</sup>, 0.1 mA h cm<sup>-2</sup>. Among them, the cells using the trisubstituted C3 and tetrasubstituted C1 electrolytes show highest CEs whereas the commonly used C2 shows



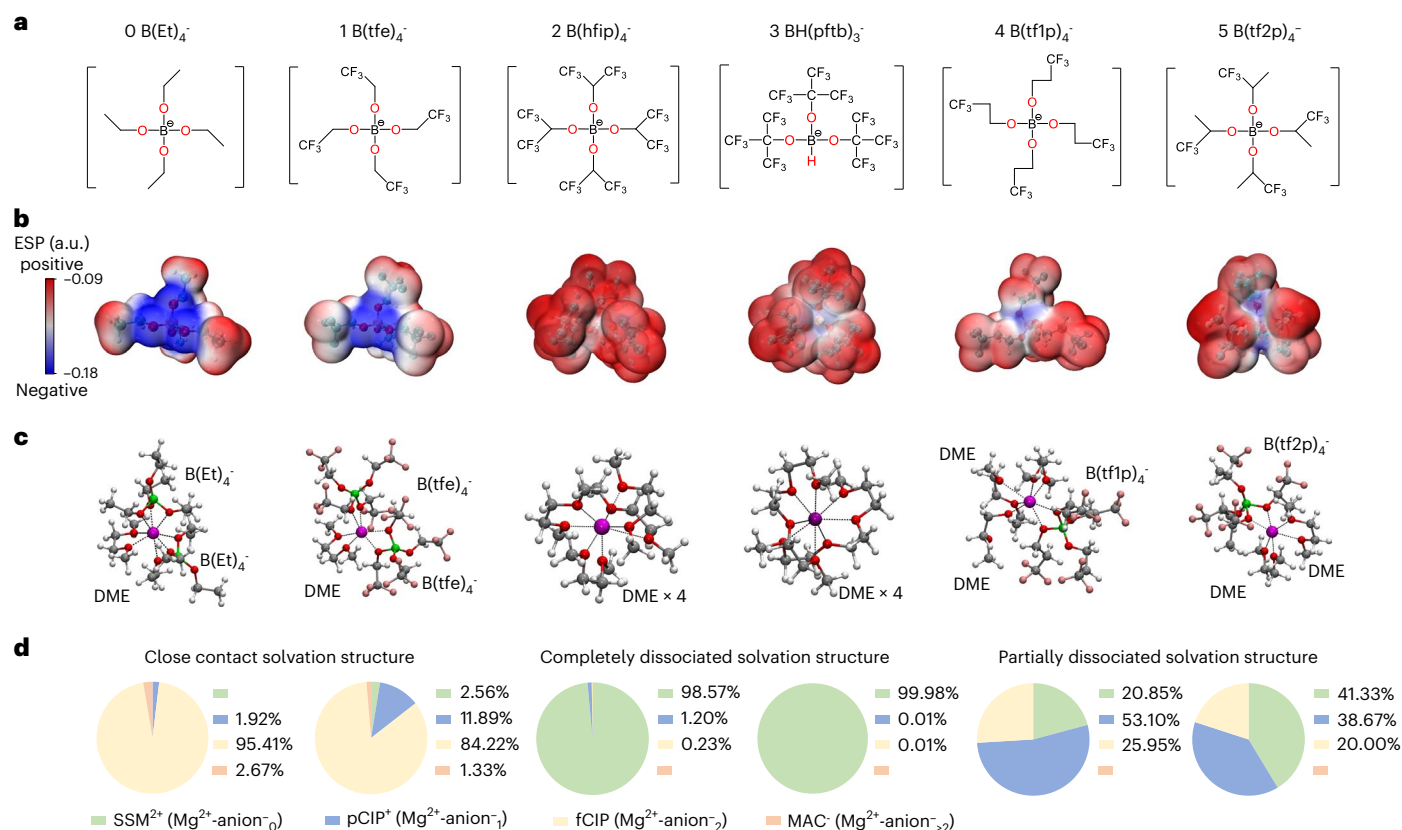


**Fig. 2 | Simulation of the solvation shell. a**, Molecular structure of six anions. **b**, Calculated ESP maps of anions under DME conditions. **c**, Typical solvation structure for the primary Mg<sup>2+</sup> solvation shell obtained from MD simulations. Colour scheme of molecules: Mg, purple; F, pink; O, red; C, grey; B, green; and H, white. **d**, Distribution of the Mg<sup>2+</sup> solvates for the six electrolytes.

the lowest CE and increasing voltage hysteresis during cycling (Supplementary Fig. 23). The Mg/Cu cells using different Mg single salts exhibit disparate performances. Under the conditions of 0.67 mA cm<sup>-2</sup> and 0.11 mA h cm<sup>-2</sup>, the cells using the M2 and M3 electrolytes show the highest CE (close to 100%) and the longest cycle life (8,400 and 2,960 cycles), whereas the cells using M4/M5/M1 have medium reversibility values of 95.61%, 93.71% and 92.68% within 600 cycles (Fig. 3b and Supplementary Fig. 24). The cycling performance and voltage hysteresis of different electrolytes are shown in Supplementary Fig. 25. C3 and M2 are chosen for deeper investigation due to their satisfactory performance. As shown in Fig. 3c, the half cell exhibits a stable average CE of 99.04% during 1,037 cycles with a cumulative capacity of 1,037 mA h cm<sup>-2</sup> under a high current density of 5 mA cm<sup>-2</sup>. The corresponding voltage profiles display a steady ~400 mV overpotential during cycling (Fig. 3d). Cyclic voltammetry of M2 reveals a high plating/stripping current density of 25 mA cm<sup>-2</sup> with a low overpotential (<350 mV) at a scan rate of 35 mV s<sup>-1</sup> (Fig. 3e). Linear sweep voltammetry results indicate that M2 has a high anodic stability of 4.0 V (vs Mg/Mg<sup>2+</sup>) towards common stainless steel counter electrodes. Meanwhile, C3 also shows a good anodic stability higher than 4.4 V (vs Ca/Ca<sup>2+</sup>) (Supplementary Fig. 26). The Mg/Mg symmetric cell using the M2 electrolyte was tested under harsh conditions (25 mA cm<sup>-2</sup>) after activation cycles. The cell exhibits a moderate overpotential (850 mV) and a long lifetime of more than 860 cycles with a cumulative capacity of 480 mA h cm<sup>-2</sup> (Fig. 3f). The high areal capacity test also proves the compatibility of M2 with the Mg metal anode under 6 mA h cm<sup>-2</sup> conditions (Supplementary Fig. 27). In addition, the Ca/Ca symmetric cell using the C3 electrolyte shows a 270 cycles lifetime (67.5 mA h cm<sup>-2</sup> cumulative capacity) with a low overpotential of ~300 mV during cycling, which is much better

than other Ca electrolytes and the results reported in other studies (Fig. 3g, Supplementary Fig. 28 and Supplementary Table 1).

The surfaces of cycled Mg and Ca (anion 1 to 5) were characterized by X-ray photoelectron spectroscopy (XPS) to determine the decomposition behaviour of different electrolytes (Fig. 3h–j). Anions 1 to 5 are selected for deeper investigation due to their satisfied cycling lifespan. Mg solvates, in particular solvates 1, 2, 4 and 5, possess almost the same decomposition products after 20 cycles in symmetric cells. Both organic (C–O, B–O, C–F) and inorganic (Mg–F/Mg–O) components from the decomposition of Mg solvates and the DME solvent can be detected (Supplementary Fig. 29). The condition becomes different for Ca metal in which the close-contact and partially dissociated Ca solvates (C1/C4/C5) possess higher Ca–O inorganic component whereas completely dissociated Ca solvates (C2/C3) show higher organic byproduct (C–O, poly C–O in C1s and O1s) in passivation layer (Supplementary Fig. 30). Moreover, for the trisubstituted M3/C3 solvates, the retained B–H structure further promotes the generation of organic B–H and inorganic metal hydrides (revealed by time-of-flight secondary ion mass spectrometry later) in the passivation layer, which are regarded as the low-migration-barriers passivation component to protect the metal anode. The decomposition species, including C–O, B–O, Mg<sup>2+</sup> and Ca<sup>2+</sup> components, were normalized by Mg<sup>0</sup> and Ca<sup>0</sup> peaks to obtain the total relative concentrations (Supplementary Table 2) in which the concentration of Ca byproducts show inverse correlation with Ca CEs (Supplementary Fig. 31). However, no similar trend is observed in the Mg metal anode, indicating that the reversibility of Ca metal is more sensitive to passivation.

TOF-SIMS gives a more intuitive element distribution in depth. For Mg solvates (Supplementary Fig. 32), the organic components (C<sub>2</sub>H<sub>3</sub>O<sub>2</sub><sup>-</sup>) and inorganic components (MgBF<sub>2</sub>O<sub>2</sub><sup>-</sup>, MgH<sup>+</sup>, MgO<sup>-</sup>) are

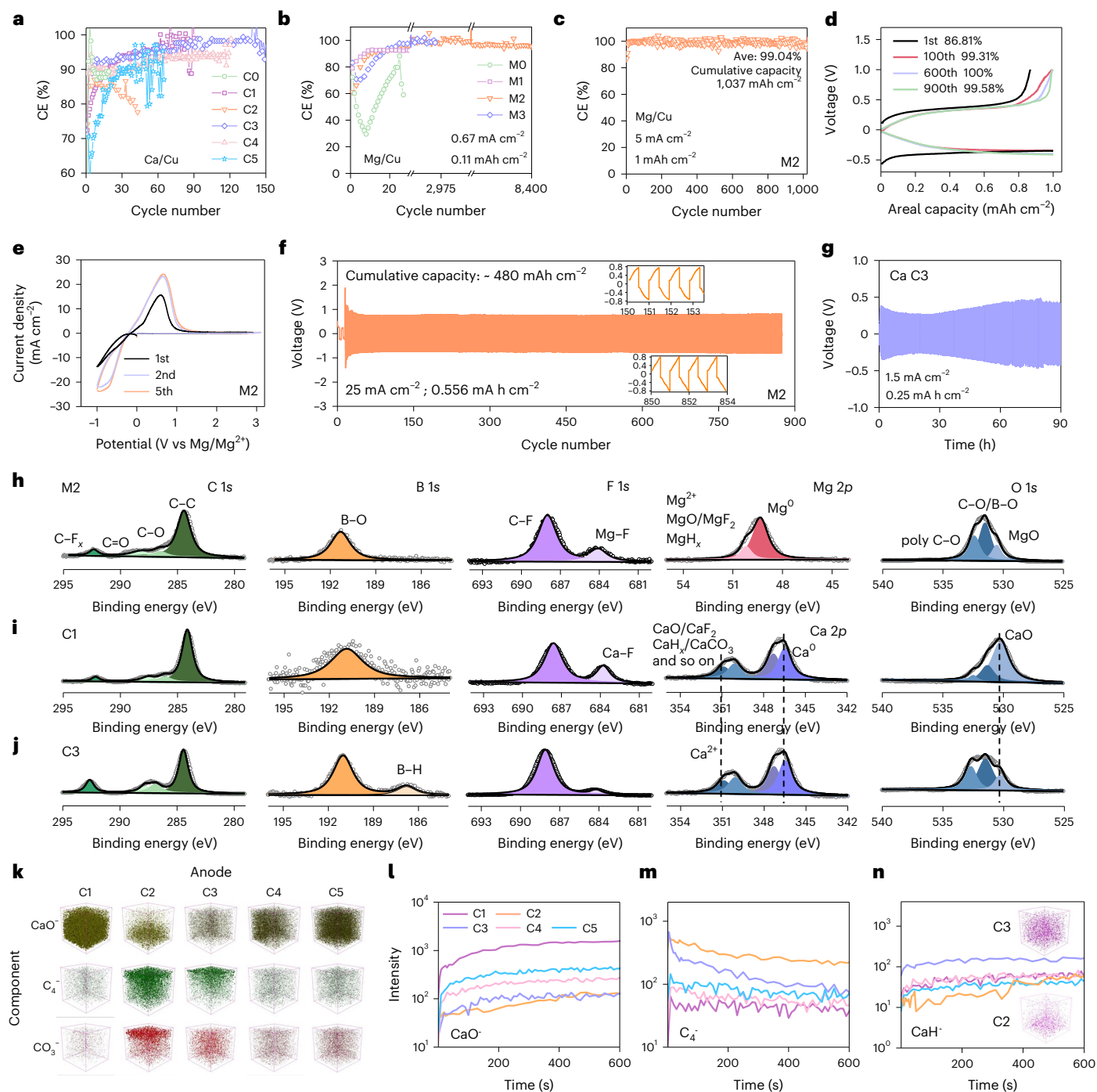


**Fig. 3 | Electrochemical performance of Ca/Mg solvates and passivation layer analysis.** **a**, Cycling performance of Ca/Cu cells using different Ca electrolytes under the conditions of  $2 \text{ mA cm}^{-2}$  and  $0.1 \text{ mA h cm}^{-2}$ . **b**, Cycling performance of Mg/Cu cells using different Mg electrolytes under the conditions of  $0.67 \text{ mA cm}^{-2}$  and  $0.11 \text{ mA h cm}^{-2}$ . (Broken linear time axes are used to present the final lifetime of different Mg electrolytes. Full data can be found in Supplementary Fig. 24). **c, d**, CE (**c**) and corresponding voltage profiles (**d**) of the cell using the M2 electrolyte under harsh conditions of  $5 \text{ mA cm}^{-2}$  and  $1 \text{ mA h cm}^{-2}$ .

**e**, Cyclic voltammogram of the Mg/Cu cell using M2 at a scanning rate of  $35.0 \text{ mV s}^{-1}$ . **f**, Mg/Mg symmetric cell using the M2 electrolyte cycled under a high current density of  $25 \text{ mA cm}^{-2}$ . (Inset graphs represent the enlarged voltage curves during cycling). **g**, Performance of the Ca/Ca symmetric cell using the C3 electrolyte. **h–j**, XPS spectra of the cycled Mg/Ca anode in the M2/C1/C3 electrolyte after 30 cycles. **k–n**, TOF-SIMS spectra (**k**) and element intensity evolution of the cycled C1–C5 anode (**l–n**).

sparsely distributed on each Mg surface. The intensities of the passivation produced by the five electrolytes are almost on the same order of magnitude (Supplementary Fig. 33), indicating the similar decomposition degree regardless of different solvation structures. Due to the higher reducibility of calcium metals, the passivation of calcium is more complex than that of magnesium (Fig. 3k–n and Supplementary

Figs. 34 and 35). A large amount of CaO was observed throughout the entire cube (C1/C4/C5), indicating that the strong anion coordinating promoted the  $\text{Ca}^{2+}$ –O interaction and facilitate the formation of CaO, which is consistent with the results observed by XPS. As a comparison, organic components ( $\text{C}_4^-$ ,  $\text{C}_2\text{HO}^-$ ) and inorganic  $\text{CaCO}_3/\text{CaF}_2$  are easily observed in completely dissociated C2 in which the formation of  $\text{CaCO}_3$

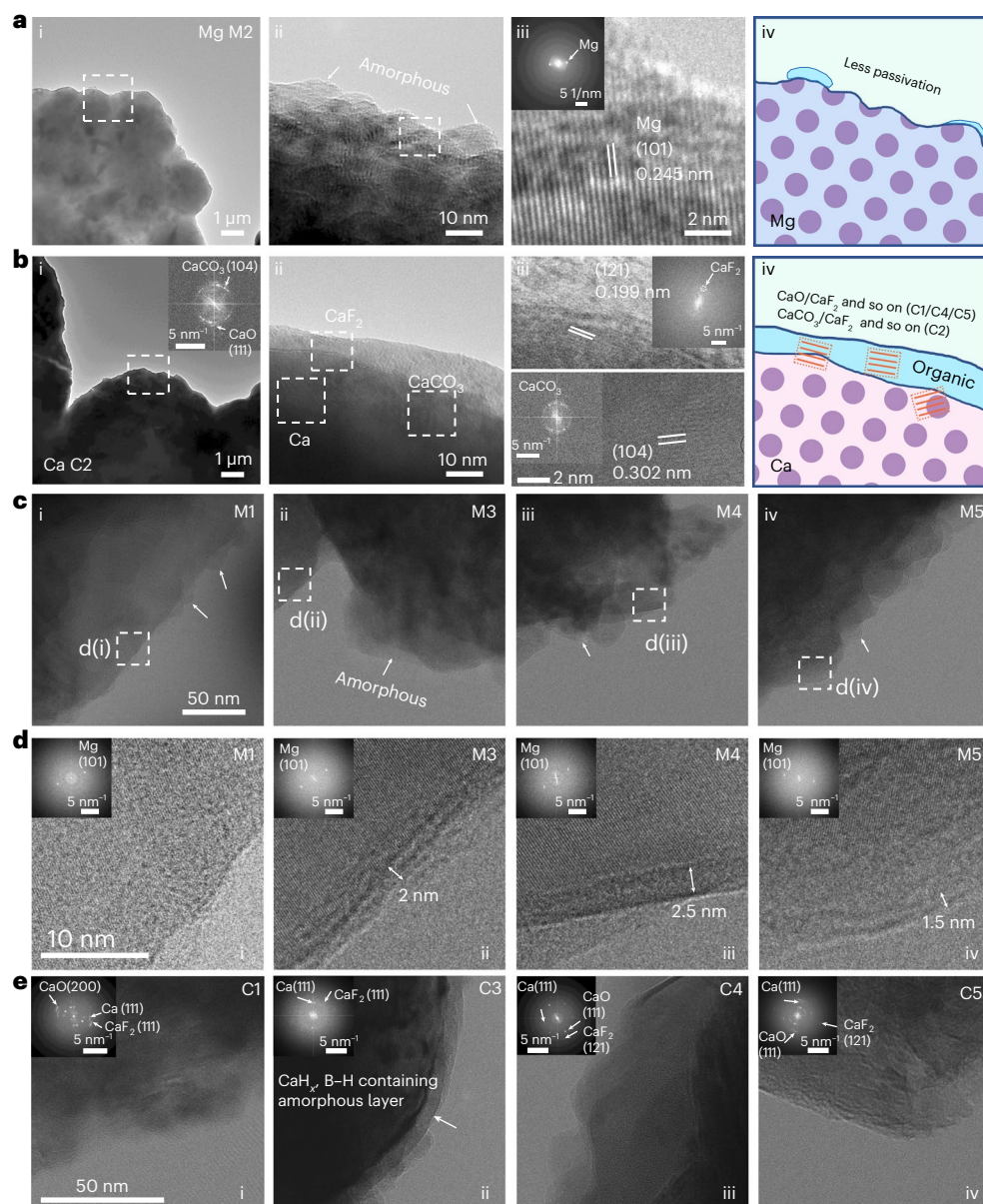


**Fig. 4 | Characterizations of the passivation layer on the Mg/Ca anode.**

**a**, Nanostructure of Mg deposited in the M2 electrolyte imaged by cryo-EM.  
**b**, Nanostructure of deposited Ca and the passivation layer in the C2 electrolyte.  
**c**, Structure of deposited Mg in the M1/M3/M4/M5 electrolytes (arrows refer

to amorphous passivation layers). **d**, Lattice fringes and FFT diffraction of deposited Mg. **e**, Nanostructure of deposited Ca and FFT diffraction of passivation components in the C1/C3/C4/C5 electrolytes.

and  $\text{CaF}_2$  can be attributed to the continuous decomposition of DME and solvate. Interestingly, although the passivation layer of C3 is mainly composed of organic components, a higher intensity of  $\text{CaH}_x$  rather than  $\text{CaCO}_3$  is observed when compared with other Ca electrolyte and unrecycled Ca anode, indicating that high concentration of  $\text{CaH}_x$  and B–H species will effectively suppress the subsequent electrolyte reduction. Considering that the migration energy barriers of  $\text{CaO}$  (997 meV) and  $\text{CaH}_2$  (541 meV) are much lower than those of  $\text{CaCO}_3$  (1,436 meV) and  $\text{CaF}_2$  (2,046 meV) (ref. 34), we believe that the passivation layer of C1, C3, C4 and C5 will be more conducive to the transport of calcium ions, thereby preventing the continuous increase of overpotential and calcium deactivation.

### Microstructure of the passivation layer

In contrast to alkali metals (Li, Na) with solid–electrolyte interphase (SEI) structures, the surface microstructure of multivalent metals remains a mystery, and until now, determining the SEI structure in

different electrolyte systems has been difficult<sup>35–40</sup>. Here we systematically characterized the Mg and Ca interfaces in various electrolyte systems through cryo-electron microscopy (cryo-EM) and identified the components in the passivation layer. As shown in Fig. 4a, Mg deposited ( $0.5 \text{ mA h cm}^{-2}$ ) in the M2 electrolyte shows a polygonal structure with a diameter larger than  $8 \mu\text{m}$ . As the magnification is increased, the lattice fringe of  $0.245 \text{ nm}$  is identified by the fast Fourier transform (FFT) pattern, corresponding to the (101) plane of metallic Mg. Interestingly, small amorphous byproducts are sparsely distributed outside the lattice fringes of bulk metallic magnesium, which proves that magnesium metal does not produce a conformal SEI structure in the highly stable organoborate/ether system, which is different from Li/Ca analogues. This random distribution structure also implies that the ion transport properties rather than passivation have large impact on Mg reversibility. The less passivation property is also detected in the enlarged images of M1/M3/M4/M5 systems. The Mg (101) plane clearly extend to the surface of the deposits in M1 and thin amorphous byproducts



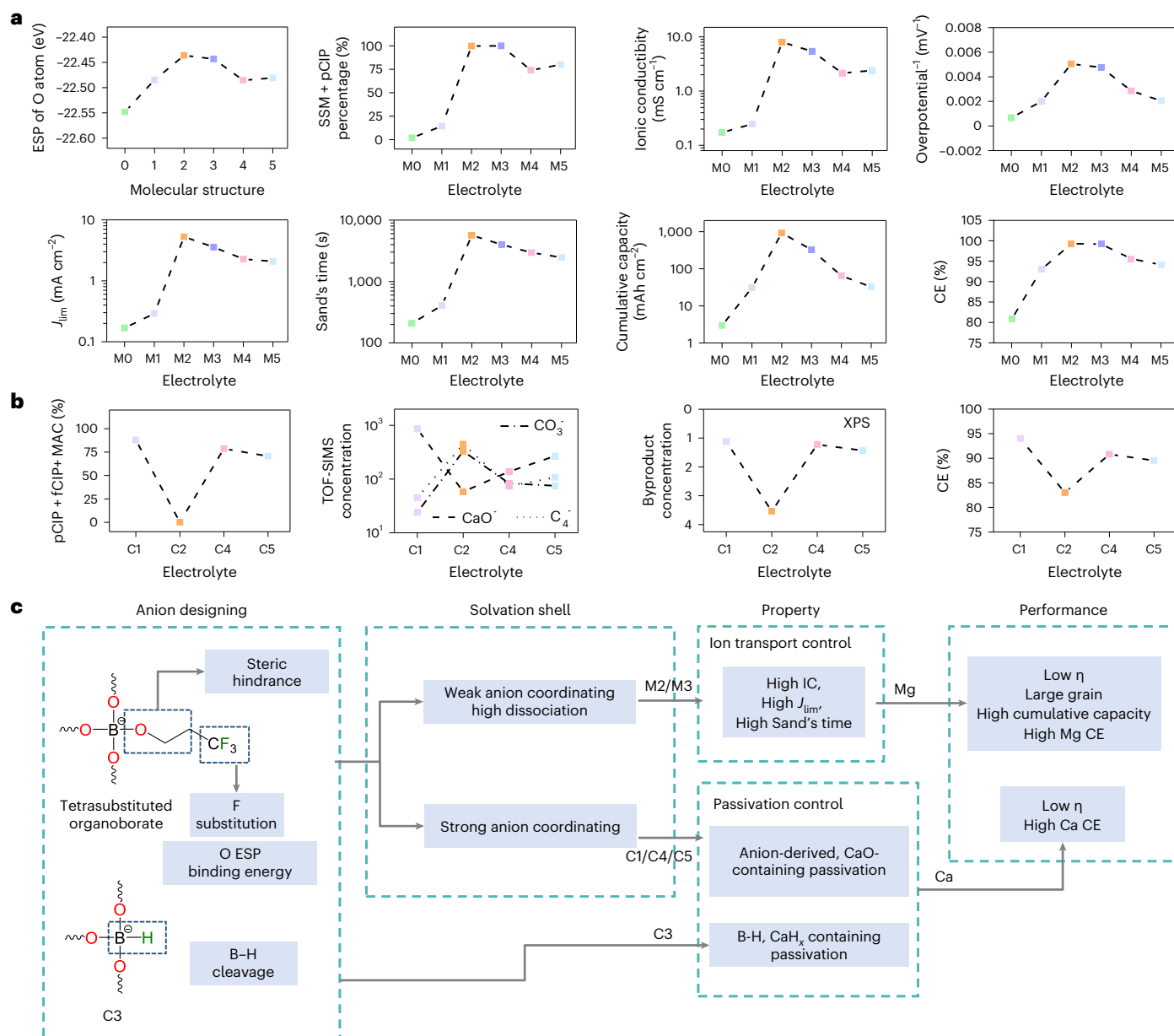


**Fig. 5 | Correlation between the molecular structure and properties and performance. a**, Correlation between the molecular design, solvation shell, Mg electrolyte transport properties and cell performance. **b**, Correlation between the solvation shell, Ca passivation layer and cell performance. **c**, Top-down design for high-performance magnesium/calcium solvates: by rationally

manipulating the chain length and F substitution at molecular level, some physico-chemical properties of solvates such as solvation capability, binding energy and ionic conductivity (IC) can be fine tuned, which influence subsequent electrolyte ion transport and SEI formation.

(<2.5 nm) are found in M3–M5 (Fig. 4c,d). In contrast, the Mg cycled in the  $\text{Mg}(\text{TFSI})_2/\text{DME}$  electrolyte exhibits a messy and irregular surface with an impurity layer ( $\text{MgF}_2/\text{MgO}$ ) of 100 nm (Supplementary Fig. 36), which blocks ion transport and results in large overpotentials and low magnesium utilization. The passivation layer becomes thinner in the  $\text{Cl}^-$ -containing electrolyte with few  $\text{MgF}_2$  nanocrystals, indicating that  $\text{Cl}^-$  can suppress the decomposition of the  $\text{TFSI}^-$  anion to some extent (Supplementary Fig. 37).

The surface of the deposited Ca metal exhibits different nanoscopic structures under the different solvation structures (Fig. 4b,e). In the completely dissociated C2 electrolyte, the calcium metal deposition mainly grows in a spherical shape with an amorphous passivation layer. The (111) Ca plane can be clearly observed (Supplementary Fig. 38), whereas many  $\text{CaCO}_3$ ,  $\text{CaF}_2$  nanocrystals are embedded

inside the amorphous layer (Supplementary Fig. 39). The passivation on C3 electrolyte also shows amorphous property with little inorganic  $\text{CaF}_2$  inside, which means B–H species and  $\text{CaH}_x$  exist in an amorphous form. In the close-contact C1 and partially dissociated C4 and C5, a polycrystalline nature of inorganic nanoparticles ( $\text{CaO}/\text{CaF}_2$ ) with fewer amorphous components can be seen (Supplementary Fig. 40), indicating an anion-derived film-formation behaviour. The different passivation species on the Ca anode are consistent with previous XPS and TOF-SIMS results.

To summarize, although some decomposition products of magnesium electrolyte are observed in XPS and TOF-SIMS, they are mainly randomly distributed rather than a conformal SEI on Mg surface, providing limited protection for the Mg plating/stripping. Moreover, a large amount of inorganic/organic decomposition products have been

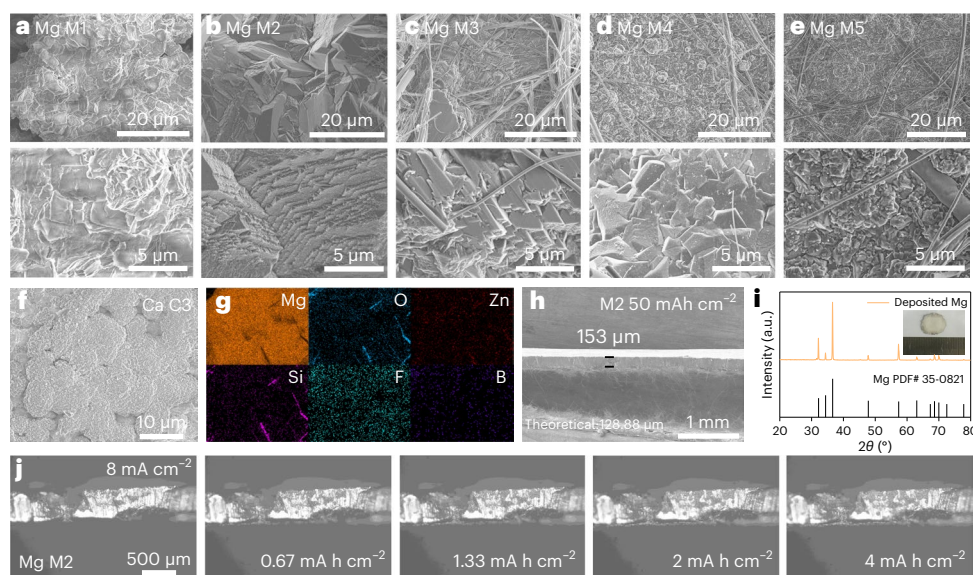


**Fig. 6 | Deposition morphology and behaviour.** **a–e**, SEM and zoomed-in images of Mg plated on a Cu substrate in the M1 (**a**), M2 (**b**), M3 (**c**), M4 (**d**) and M5 (**e**) electrolytes under the conditions of 1 mA cm<sup>−2</sup> and 5 mA h cm<sup>−2</sup>. **f**, SEM images of Ca plated on a Cu substrate in C3 under the conditions of 0.5 mA cm<sup>−2</sup> and

0.5 mA h cm<sup>−2</sup>. **g**, EDS mapping of the Mg deposits on the Cu substrate. **h**, Cross-sectional SEM image of Mg with an areal capacity of 50 mA h cm<sup>−2</sup>. **i**, XRD pattern of deposited Mg. The inset shows a digital photo of deposited Mg. **j**, Smooth Mg deposition behaviour revealed by in situ optical microscopy under 8 mA cm<sup>−2</sup>.

observed on the surface of calcium metal, and their relative content is mainly related to the solvation structure and anion structure, which will affect subsequent electrochemical performance.

### Anion design–solvation shell–property correlation

In addition to the passivation layer, another factor critical to the battery performance is the electrolyte transport properties. Considering the similarity of the solvation shell of Mg and Ca in DFT simulations, we took the example of Mg metal to investigate the ion transport properties of different electrolytes. Cation transference numbers ( $t_+$ ) of six electrolytes were measured and found that the values were mainly concentrated between 0.3 and 0.5 (Supplementary Fig. 41). After obtaining  $t_+$  and ion conductivity, the parameters of apparent diffusion coefficient ( $D$ ), critical current density ( $j_{lim}$ ) and Sand's time ( $\tau$ ) can be calculated by using Einstein–Nernst equation (1), critical current density equation (2) and the Sand equation (3).

$$\sigma_+ = \sigma t_+ = \frac{CDF^2z^2}{RT} \quad (1)$$

$$j_{lim} = \frac{CD}{1-t_+} \frac{2F}{L} \quad (2)$$

$$\tau^{0.5} = \frac{zFACD^{0.5}\pi^{0.5}}{2i(1-t_+)} \quad (3)$$

Where  $\sigma_+$  is cation conductivity,  $\sigma$  is ionic conductivity,  $C$  is the bulk cation concentration,  $F$  is the Faraday constant,  $z$  is the number of electrons transferred,  $R$  is the gas constant,  $T$  is temperature,  $L$  is the diffusion length,  $A$  is the electrode area and  $i$  is the applied current.

Under the premise of small differences in  $t_+$ , there is a positive correlation between ionic conductivity and diffusion coefficient/critical current density/Sand time ( $\sigma \propto D \propto j_{lim}$  and  $\tau$ ; Supplementary Fig. 42). Considering the passivation layer in M1–M5 does not effectively protect the magnesium anode, the ionic conductivity directly determines the time of dendrite formation and cell lifespan. This view

was confirmed by galvanostatic polarization (Supplementary Fig. 43), half-cell cycling and deposition characterization from which many dead Mg in low-ionic-conductivity electrolyte (M1) can be seen, and the diameter of Mg is also smaller than that in M2–M5.

On the basis of the abovementioned experimental and simulation results, we summarize an interesting anion design–solvation structure–property/performance relationship (Fig. 5a–c) from which we believe that the electrochemical performance using Mg organoborate is mainly controlled by ion transport, whereas the electrochemical performance using Ca organoborate is more affected by passivation components.

For Mg metal, the large and high-F-substitution design improves the dissociation degree in solvation shell, which directly affects kinetics parameters such as ionic conductivity ( $\sigma$ ), apparent diffusion coefficient ( $D$ ), limiting current density ( $j_{lim}$ ) and Sand's time ( $\tau$ ) in the battery. The higher ionic conductivity (for example, M2, M3) provided fast cation diffusion and high limiting current density, which decreases the concentration gradient approaching the electrode surface, making the electrodeposition to exhibit a large polyhedral grain under kinetic control. This morphology avoids the formation of dead metal and dendrite during cycling (Supplementary Fig. 44), which directly affecting the Mg CEs and cell lifespan. Although a small number of byproducts are found on the Mg surface, the random distribution rather than conformal SEI structure makes the Mg passivation layer providing less impact on Mg reversibility.

However, for calcium metal, the complicated passivation components make the failure mode of Ca metal more complex (Fig. 5b and Supplementary Fig. 45). Although we can observe the short-circuit behaviour obey the Sand's time rule with a rank of C3 > C4 / C5 > C1 in symmetrical cells, their CE and ion transport properties are not directly related. Combining TOF-SIMS and electrochemical performance, we found reducing the formation of high-migration-barriers byproducts (for example CaCO<sub>3</sub>, CaF<sub>2</sub>)<sup>34</sup> and preventing Ca deactivation are the key to improving the reversibility of calcium metals. One way is to establish an anion-participating solvation structure using small and low-F-substitution design (for example, C1/C4/C5, C0 is not included due to limited lifetime). Higher fCIP and pCIP<sup>+</sup> in the primary solvation shell means that anions dominate the formation of the passivation layer rather than DME, thus promoting the Ca<sup>2+</sup>–O interaction and forming



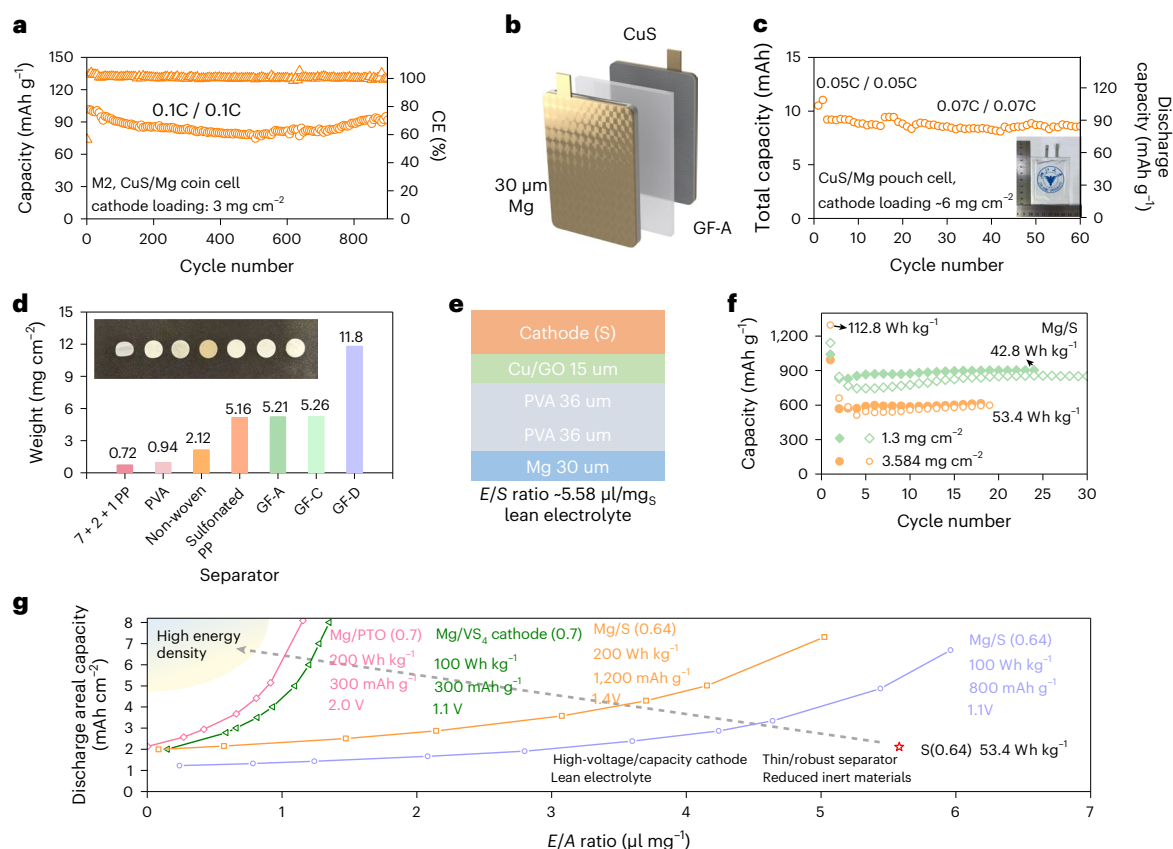


**Fig. 7 | Electrochemical performance of Mg metal full cells and the pathway towards high energy density.** **a**, Cycling performance of a Mg/CuS coin cell using the M2 electrolyte under 0.1 C. **b**, Schematic of a conventional Mg metal pouch cell coupled with a 30-μm metal anode and a CuS cathode. **c**, Cycling performance of the CuS/Mg pouch cell under flooded electrolyte conditions. **d**, Selection of a thin/Mg compatible separator (7+2+1 PP: 7 μm polypropylene, 2 μm boehmite coating, 1 μm polymer coating. GF-A, GF-C, GF-D: The types of

glass microfiber filters). **e**, Configuration of high-energy-density Mg/S cells coupled with a GO/Cu interlayer, a thin PVA separator and a lean electrolyte. **f**, Cycling performance of 42.8 and 53.4 Wh kg<sup>-1</sup> Mg/S coin cells at 0.1 C at 60 °C. **g**, Pathway towards high-energy-density Mg metal cells using a high-voltage/high-capacity cathode, a lean electrolyte and a limited anode (E/A ratio: electrolyte weight to active mass; the discharge capacity, active mass ratio and average voltage for calculation are listed in the figure).

the CaO-based passivation rather than organic/solvent-derived CaCO<sub>3</sub> components. We also examined the Ca/Cu cells using 0.15 M and 0.5 M Cl<sup>-</sup> and found that low-concentration Cl<sup>-</sup> shows a low CE and a short lifetime trend, similar to C2 (Supplementary Fig. 46). Considering that the maximum solubility of C2 is 0.5–0.6 M, obtaining a stable anion-derived passivation layer and a high CE in the C2 system is almost impossible. The other way is to design the molecular with active B–H bond, which can easily cleavage to form low-migration-barrier CaH<sub>x</sub> and B–H containing passivation, blocking the subsequent solvent reduction reactions.

## Divalent metal electrodeposition morphology

Scanning electron microscopy (SEM) and in situ optical microscopy measurements were carried out to observe the metal deposition behaviour. First, we deposited 5 mA h cm<sup>-2</sup> fresh Mg on a Cu current collector using currently available electrolytes, including M0–M5, Mg(TFSI)<sub>2</sub>, Mg(TFSI)<sub>2</sub> + Cl<sup>-</sup>, MgCl<sub>2</sub>/AlCl<sub>3</sub> (MACC) and Mg(TFSI)<sub>2</sub> + methoxyethyl-amine chelants in DME. As shown in Fig. 6a–e, the surface of M2 exhibits a dendrite-free, smooth morphology, and the magnified image below shows a lamellar structure with epitaxial growth behaviour. The cells using other organoborate electrolytes also exhibit compact Mg deposition, whereas the diameter of deposits gradually decreases (M2 > M3 > M4 > M5 ≈ M1 > M0) according to their ionic conductivity. As a comparison, Mg(TFSI)<sub>2</sub>-based and MACC electrolytes show a messy deposition with a rough interface

even when adding effective additives such as 3-methoxypropylamine and Cl<sup>-</sup>, which means that a high CE does not imply a better deposition morphology (Supplementary Fig. 47). Compared with Mg metal, Ca electrodeposition in the C3 electrolyte exhibits small agglomerates with a rough surface, which may be attributed to the more intense reaction between the calcium metal and electrolyte and the thicker passivation layer (Fig. 6f). Energy-dispersive spectrometry (EDS) mapping proves the successful electrodeposition of Mg/Ca in different electrolytes with passivation derived from salt/solvent decomposition (Fig. 6g and Supplementary Fig. 48). Cross-sectional SEM also exhibits uniform and dense Mg electrodeposition with a thickness of 153 μm after 50 mA h cm<sup>-2</sup> deposition (Fig. 6h), which is close to the theoretical thickness (1 mA h cm<sup>-2</sup> = 2.5776 μm Mg). The digital photo and X-ray diffraction (XRD) pattern of deposited Mg show a white surface with an optimal (101) texture (Fig. 6i). Optical microscopy also demonstrated a dense Mg deposition without obvious dendrite-like Mg growth (Fig. 6j and Supplementary Fig. 49).

## Cycling performance of the Mg full cell

To achieve high-energy-density practical Mg metal batteries, some important parameters already used in Li-metal/Li-ion batteries need to be carefully controlled, such as the N/P ratio (negative-to-positive electrode capacity ratio) and E/C ratio (electrolyte weight to cathode capacity ratio), which are related to the capacity/loading of the metal anode and cathode, the thickness of the separator and the weight of

the electrolyte<sup>41–43</sup>. In this section, we investigated the full-cell performance of the synthesized electrolytes using different cathodes and thin separators and explored the possibility of reaching 200 Wh kg<sup>-1</sup>.

First, CuS/Mg coin batteries were assembled to investigate the cycling performance under mild conditions. As shown in Fig. 7a and Supplementary Fig. 50, the commercial CuS cathode shows a capacity of ~100 mA h g<sup>-1</sup> (0.3 mA h cm<sup>-2</sup>) for Mg<sup>2+</sup> storage in both the M2 and M3 electrolytes. The cell cycling in M2 exhibits a 95% capacity retention after 900 cycles under 0.1 C charge/discharge conditions, whereas that using M3 exhibits a 63% capacity retention after 130 cycles. Moreover, we also used an ultrathin Mg foil (30 μm) anode and a thin GF-A separator to fabricate the CuS/Mg pouch cell to evaluate the performance of M2 at a large scale (Fig. 7b and Supplementary Fig. 51). The capacity of the ultrathin Mg foil is approximately 10.996 mA h cm<sup>-2</sup> (Supplementary Fig. 52), and that of the CuS cathode used in the pouch cell is approximately 6 mg cm<sup>-2</sup>. The pouch cell shows a total capacity of 9.2 mA h after activation and maintains a 93.2% capacity retention after 60 cycles (Fig. 7c and Supplementary Fig. 53).

For high-energy-density configuration, pyrene-4,5,9,10-tetraone (PTO) with enolization redox chemistry and S with conversion-type chemistry were investigated (Supplementary Fig. 54). The PTO/Mg/M2 cell exhibits an acceptable capacity of 260 mA h g<sup>-1</sup> with an average discharge voltage of ~2 V under low active mass loading (1 mg cm<sup>-2</sup>) and 30% active mass conditions (Supplementary Fig. 55). However, its low tap density and high porosity make high energy density an extravagant hope (Supplementary Fig. 56). As of now, we have inferred that the PTO/Mg configuration will have difficulty obtaining a high energy density unless high tap density and a high-pressure compaction electrode can be well established.

For the Mg/S system, we modified the separator and interlayer to obtain a high-energy and stable cycling performance. A thickness-controllable PVA separator was prepared by electrospinning, which can be easily infiltrated by a lean electrolyte (Supplementary Figs. 57 and 58). Compared with GF-A (5.21 mg cm<sup>-2</sup>), the mass per unit area of 36 μm PVA (0.94 mg cm<sup>-2</sup>) decreases by 80% and shows compatibility with the Mg metal anode (Fig. 7d and Supplementary Fig. 59). Moreover, a GO layer with embedded Cu nanoparticles was prepared by filtration, which can suppress the shuttle effect of polysulfides and improve the cycling stability (Supplementary Figs. 60 and 61). With these efforts, high-energy-density Mg metal prototypes were fabricated using a lean electrolyte and a high-loading S cathode at 60 °C. The detailed structure is displayed in Fig. 7e. The coin cell with 1.3 mg<sub>s</sub> loading ( $E/S = 11.5 \mu\text{l mg}^{-1}$ ) exhibits an initial capacity of ~1,141 mA h g<sup>-1</sup> with a 74.6% capacity retention after 30 cycles (Fig. 7f). The corresponding energy densities of the two parallel cells are 42.8 Wh kg<sup>-1</sup> and 41.4 Wh kg<sup>-1</sup>. When using a high-loading cathode (3.584 mg<sub>s</sub>) and a high-loading GO/Cu interlayer, the cells ( $E/S = 5.58 \mu\text{l mg}^{-1}$ ) exhibit an energy density of ~53.4 Wh kg<sup>-1</sup> and 52.1 Wh kg<sup>-1</sup> after ~19 cycles (the energy density of first cycle is 112.8 Wh kg<sup>-1</sup> and 86.5 Wh kg<sup>-1</sup> for two parallel cells). This stable cycling performance is derived from both the Mg/S (~1.5 V) and Cu<sub>x</sub>S/Mg (~1.1 V) chemistry under higher temperature. The detailed parameters for these Mg coin cells are listed in Supplementary Table 3 and Supplementary Fig. 62.

In short, the realization of high-energy-density magnesium metal batteries still requires joint efforts and attention (Fig. 7g). First, the capacity of Mg/S cells rapidly decays, and there is an urgent need to find stable and high-capacity cathodes (for example, Mg<sub>0.15</sub>MnO<sub>2</sub> or VS<sub>4</sub>) for a high-energy-density configuration. Second, lean electrolyte is also needed for higher energy density, and there is an urgent need to find a high-boiling-point solvent (>90 °C) that is suitable for both Mg anode and pouch cell configurations. Third, high cathode loading requires a suitable/rigid separator to suppress the penetration of magnesium metal and prevent short circuits.

## Conclusions

In this work, we prepared high-performance Mg/Ca organoborate salts through a facile cation replacement method using an inexpensive Zn(BH<sub>4</sub>)<sub>2</sub> precursor. By exploiting the high metal activity of Mg and Ca, Zn<sup>2+</sup> in the solvation structure can be easily replaced to obtain desired solvates. By combining MD/DFT calculations with experimental results, we elucidated the anion design–solvation structure–property/performance relationship. Specifically, by rationally designing the chain length and F-substitution degree of precursors, the solvation shell, ionic conductivity, interfacial properties and cycling performance can be well tuned. A completely dissociated magnesium organoborate system (M2) provides a thin passivation interface with a 99.04% CE, and the calcium organoborate systems (C1/C3) with close-contact solvation or B–H inclusion properties offers CaO/CaH<sub>x</sub>-based passivation layer with high reversibility. By using a 30 μm Mg anode, a low electrolyte/sulfur ratio ( $E/S = 5.58 \mu\text{l mg}^{-1}$ ), a modified PVA separator and a GO/Cu interlayer, a rechargeable 53.4 Wh kg<sup>-1</sup> Mg metal prototype is achieved. Drawing on our collective findings, we discussed challenges and possible pathways towards high-energy-density magnesium batteries beyond 100 Wh kg<sup>-1</sup>. Our results pave the way for realizing next-generation earth-abundant, energy-dense multivalent metal-ion technologies.

## Methods

### General

1 M Zn(BH<sub>4</sub>)<sub>2</sub>/THF was purchased from Rhawn Chemical Reagent Network. Hexafluoroisopropanol was purchased from Adamas-beta. Perfluoro-tert-butanol was purchased from Energy Chemical. Ethanol, 2,2,2-trifluoroethanol, 3,3,3-trifluoro-1-propanol, 1,1,1-trifluoro-2-propanol and 3-Methoxypropylamine (MPA) were purchased from Shanghai Aladdin Biochemical Technology Co. Mg(TFSI)<sub>2</sub> was purchased from Dodochem Co. and used as received. 1,2-Dimethoxyethane (DME) was provided by Shanshan Advanced Materials (Quzhou) Co. 3 N Mg foils and hexane were purchased from Sinopharm Chemical Reagent Co. 1-mm-thick Ca foils were purchased from zkynxc.com. 30-μm Mg foil was purchased from Ningjin County Huabeimei Processing Factory. Ca granules, AlCl<sub>3</sub>, MgCl<sub>2</sub>, ZnCl<sub>2</sub>, CuS and nano Cu powder were purchased from Shanghai Macklin Biochemical Co. Pyrene-4,5,9,10-tetraone was purchased from aikonchem Co.

### Synthesis of Mg and Ca solvates and electrolyte

**Processes.** Mg(B(Et)<sub>4</sub>)<sub>2</sub> and Ca(B(Et)<sub>4</sub>)<sub>2</sub>: in a typical process, 2 ml Zn(BH<sub>4</sub>)<sub>2</sub>/THF solution (2 mmol) was dissolved into 2 ml DME in a glass bottle after which 0.737 g (16 mmol) ethanol was gradually added with stirring. The solution was stirred more than 24 h, and Mg or Ca foils were immersed into solution to replace the solvated Zn<sup>2+</sup> to Mg<sup>2+</sup>/Ca<sup>2+</sup> until the surface without any black Zn appeared. The obtained transparent solution was purified by ethanol again to remove the remaining the BH<sub>4</sub><sup>-</sup>. Finally, the solution was dried in vacuo under room temperature for two hours to obtain the target solvate.

Mg(B(tfe)<sub>4</sub>)<sub>2</sub> and Ca(B(tfe)<sub>4</sub>)<sub>2</sub>: in a typical process, 2 ml Zn(BH<sub>4</sub>)<sub>2</sub>/THF solution (2 mmol) was dissolved into 2 ml DME in a glass bottle after which 1.6 g (16 mmol) 2,2,2-trifluoroethanol was gradually added with stirring. The solution was stirred more than 24 h, and Mg or Ca foils were immersed into solution without stirring until the surface without any black Zn appeared. The obtained transparent solution was purified by 2,2,2-trifluoroethanol again to remove the remaining the BH<sub>4</sub><sup>-</sup>. Finally, excessive hexane was added into solution to precipitate the target solvate. After removing the solution, the white salt was dried in vacuo under room temperature.

Mg(B(hfip)<sub>4</sub>)<sub>2</sub> and Ca(B(hfip)<sub>4</sub>)<sub>2</sub>: in a typical process, 2 ml Zn(BH<sub>4</sub>)<sub>2</sub>/THF solution (2 mmol) was dissolved into 2 ml DME in a glass bottle after which 2.689 g (16 mmol) hexafluoroisopropanol was gradually added with stirring. The solution was stirred more than 24 h, and Mg or Ca foils were immersed into solution without stirring until the surface without any black Zn appeared. The obtained transparent solution was

purified by hexafluoroisopropanol again to remove the remaining the  $\text{BH}_4^-$ . Finally, excessive hexane was added into solution to precipitate the target solvate. After removing the solution, the white salt was dried in vacuo under room temperature.

$\text{Mg}(\text{BH}(\text{pftb})_3)_2$  and  $\text{Ca}(\text{BH}(\text{pftb})_3)_2$ : in a typical process, 2 ml  $\text{Zn}(\text{BH}_4)_2/\text{THF}$  solution (2 mmol) was dissolved into 2 ml DME in a glass bottle after which 2.832 g (12 mmol) perfluoro-tert-butanol was gradually added with stirring. The solution was stirred more than 24 h, and Mg or Ca foils were immersed into solution without stirring until the surface without any black Zn appeared. The obtained transparent solution was purified by perfluoro-tert-butanol again to remove the remaining the  $\text{BH}_4^-$ . Finally, excessive hexane was added into solution to precipitate the target solvate. After removing the solution, the white salt was dried in vacuo under room temperature.

$\text{Mb}(\text{B}(\text{tf1p})_4)_2$  and  $\text{Ca}(\text{B}(\text{tf1p})_4)_2$ : in a typical process, 2 ml  $\text{Zn}(\text{BH}_4)_2/\text{THF}$  solution (2 mmol) was dissolved into 2 ml DME in a glass bottle after which 1.824 g (16 mmol) 3,3,3-trifluoro-1-propanol was gradually added with stirring. The solution was stirred more than 24 h and Mg or Ca foils were immersed into solution to replace the solvated  $\text{Zn}^{2+}$  to  $\text{Mg}^{2+}/\text{Ca}^{2+}$  until the surface without any black Zn appeared. The obtained solution was purified by 3,3,3-trifluoro-1-propanol again to remove the remaining the  $\text{BH}_4^-$ . Finally, the solution was dried in vacuo under room temperature for two hours to obtain the target solvate.

$\text{Mg}(\text{B}(\text{tf2p})_4)_2$  and  $\text{Ca}(\text{B}(\text{tf2p})_4)_2$ : in a typical process, 2 ml  $\text{Zn}(\text{BH}_4)_2/\text{THF}$  solution (2 mmol) was dissolved into 2 ml DME in a glass bottle after which 1.824 g (16 mmol) 1,1,1-trifluoro-2-propanol was gradually added with stirring. The solution was stirred more than 24 h and Mg or Ca foils were immersed into solution to replace the solvated  $\text{Zn}^{2+}$  to  $\text{Mg}^{2+}/\text{Ca}^{2+}$  until the surface without any black Zn appeared. The obtained solution was purified by 1,1,1-trifluoro-2-propanol again to remove the remaining the  $\text{BH}_4^-$ . Finally, the solution was dried in vacuo under room temperature for two hours to obtain the target solvate.

Preparation of 0.5 M M2 solutions: 826 mg ( $\text{Mg}(\text{DME})_3(\text{B}(\text{hfp})_4)_2$ ) was dissolved into 0.6 ml DME with stirring, then DME was dropwise added to form a 1 ml solution. Note that 0.25 M M2 electrolyte (density:  $1.07 \text{ g cm}^{-3}$ ) was used in a high-energy-density test considering of high molecular weight of M2. The other electrolytes were prepared based on the molar quantity of  $\text{Zn}(\text{BH}_4)_2$ .

Preparation of MACC solutions: 87 mg  $\text{MgCl}_2$  and 60 mg  $\text{AlCl}_3$  were added to 15 ml THF. The mixture was stirred overnight at room temperature to obtain the MACC.

Preparation of  $\text{Mg}(\text{TFSI})_2$  with multidentate methoxyethyl-amine chelants: 292 mg  $\text{Mg}(\text{TFSI})_2$  was added into solution of 0.7 ml DME and 0.3 ml MPA. The mixture was stirred overnight at room temperature.

Preparation of  $\text{Mg}(\text{TFSI})_2$  with  $\text{Cl}^-$  additive: 292 mg  $\text{Mg}(\text{TFSI})_2$  and 15 mg  $\text{ZnCl}_2$  were added into solution of 1 ml DME. The mixture was stirred overnight at room temperature.

### Preparation of electrode, separator and interlayer

The CuS cathode ( $3\text{--}6 \text{ mg cm}^{-2}$ ) was prepared using CuS, SuperP and polyvinylidene difluoride (PVDF) in an 8:1:1 mass ratio. The slurry was cast on a copper foil and dried at  $80^\circ\text{C}$  under vacuum for 12 h. For the cathode of 30% active mass ratio, PTO cathode  $\sim 1 \text{ mg}$  was prepared using PTO, SuperP and PVDF in a 3:5:2 mass ratio. For the high active mass ratio cathode, PTO and carbon nanotubes were mixed in a 4:6 or 7:3 mass ratio. The slurry was cast on an Al foil, and the electrode was pressed under the pressure of 20 MPa. The S cathode was prepared using S/C composite (0.8), SuperP and PVDF in an 8:1:1 mass ratio.

The GO/Cu film was prepared by dispersing 10 mg GO into 5 ml ethanol with the aid of ultrasonic after which a certain quantity of nano Cu particles was added into the solution for further ultrasonication. The solution was filtered through the polypropylene separator to obtain a free-standing film.

Fabrication of PVA nanofibrous separators: first, PVA was dissolved in deionized water and thoroughly stirred to form a homogenous

solution with a concentration of 10% (w/w). The prepared precursor solution was transferred to a 10 ml syringe. The electrospinning process was performed under the condition of  $30^\circ\text{C}$  and 50% humidity. The voltage applied is 18 kV, and the feed rate is  $0.3 \text{ ml h}^{-1}$ . The distance between the needle and the Al foil collector is 15 cm and the rotational speed is 300 r.p.m. The obtained PVA film was finally dried in vacuo under  $80^\circ\text{C}$  for 24 h.

**Electrochemical measurement.** The 2032 coin cells are fabricated in the argon-filled glovebox with  $\text{H}_2\text{O}$  and  $\text{O}_2 < 0.1 \text{ ppm}$ . Neware electrochemical testing systems (CT-4008T-5V10mA) were used to obtain the electrochemical performance of Mg/Ca metal-based cells. Mg foil (100  $\mu\text{m}$  and 30  $\mu\text{m}$ ) and Ca foil (500  $\mu\text{m}$ ) were polished until the surface became shiny before use. For the conventional test, glass fibre (GF-D) separator and adequate electrolytes (120  $\mu\text{l}$ ) were used for cycling. For the high-energy-density test, PVA separator, interphase layer (GO and carbon nanotube) and lean electrolytes (15–20  $\mu\text{l}$ ) were used for cycling. Asymmetric cells use Cu foils as counter electrode and cycled at 0–2 V for five cycles. After activation, Mg/Ca was plated on Cu electrode and stripped with a cut-off voltage of 1.0 or 1.4 V. CHI600E Workstation was used to evaluate the linear sweep voltammetry ( $5 \text{ mV s}^{-1}$ ) and cyclic voltammetry ( $35 \text{ mV s}^{-1}$ ) performance.

**Characterization.** The morphologies and element mapping of Mg/Ca anode were examined by SEM SU-8010 (Hitachi) at 5–15 kV. Single-crystal X-ray diffraction was performed on Gemini A OHra, Varian. Inductively coupled plasma-mass spectrometry (ICP-MS) was carried out on NexIon 300Q, PerkinElmer. Electrospray ionization-mass spectrometry (ESI-MS) was performed on 6224 TOF LC/MS, Agilent Technologies. Nuclear magnetic resonance spectra (NMR) was performed on DD2-600 (600 MHz, in  $\text{DMSO}-d_6$ ), Agilent Technologies. The surface composition was examined by X-ray photoelectron spectroscopy (ESCALAB 250Xi, ThermoFisher Scientific). Cryo-Electron Microscopy was performed on Talos F200C 200 kV. Time of flight secondary ion mass spectrometry (TOF-SIMS) was analysed by 5 iontof, PHI NanoTOFII. Optical microscopy was performed on Nikon DS TI-FL. X-ray diffraction (XRD) spectrum was performed on XRD-7000. Raman spectra were performed on ThermoFisher DXR SmartRaman.

### Simulation details

**MD simulation.** The dynamics behaviour of the solvation structures of the studied systems were predicted at Generation Amber Force Field (GAFF) force field. The Universal Force Field (UFF) force field was applied for the Lennard-Jones potential parameters of B element. The bonded parameters involving B were fitted by diagonal elements of redundant internal coordinated Hessian method with Sobtop package<sup>44</sup>. The partial charges for all molecules were computed by fitting the RESP2 (ref.<sup>45</sup>) charge of molecules at B3LYP/Def2-TZVP level. The electrostatic interactions in the systems were described by Ewald summation method. The integration for each MD step was set to 1 fs. All simulations were conducted under the NPT ensemble at 300 K. In each MD simulation, an initial equilibration period of 5 ns was used to equilibrate the system, followed by a 45 ns sampling period. All MD simulations were conducted using the GROMACS 2018 programme.

**DFT simulation.** The electrostatic potential (ESP) involved in the analyses was evaluated by Multiwfn based on the highly effective algorithm<sup>46,47</sup>. The total ESP without contribution from nuclear charge of O atom was also calculated with the Multiwfn software.

The binding energy was calculated by subtracting the reactant energies from the complex energy. The geometry of each compound was first optimized using the B3LYP functional<sup>48</sup> and the 6–31 G(d) basis set. A dispersion correction was also considered using the



Becke–Johnson damping function. The solvation effect was described with the Integral Equation Formalism variant of the Polarizable Continuum model<sup>49,50</sup>, where the static dielectric constant and dynamic dielectric constant were set to be 7.2 and 1.9 for the DME solvent, respectively. Then, the energy of each compound was calculated by the DFT method using the M06–2X functional<sup>51</sup> and def2-TZVP basis set. A dispersion correction was also considered using the zero-damping function. The solvation effect was described with the Solvation Model Based on Density<sup>52</sup>, where the static dielectric constant and dynamic dielectric constant were set to be 7.2 and 1.9 for the DME solvent, respectively.

### Calculation of energy density at cell level

To calculate the 200 Wh kg<sup>−1</sup> Mg/PTO system: the discharge capacity was assumed as 300 mA h g<sup>−1</sup>, and the discharge voltage platform was set as 2 V. Considering the high porosity and low electric conductivity of PTO, the active mass ratio was set as 70%.

To calculate the 100 and 200 Wh kg<sup>−1</sup> Mg/S system: the discharge capacity was assumed as 800/1,200 mA h g<sup>−1</sup> and the discharge voltage platform was set as 1.1/1.4 V. The active mass ratio was set as 64%. The mass of inert material is listed in Supplementary Table 3. Moreover, we did not take the mass of the packaging into these two calculations.

To calculate the 100 Wh kg<sup>−1</sup> Mg/VS<sub>4</sub> system: the discharge capacity was assumed as 300 mA h g<sup>−1</sup> and the discharge voltage platform was set as 1.1 V. The active mass ratio was set as 70%.

### Data availability

All data that support the main findings are available in the main text and the Supplementary Information.

### Code availability

The Python codes for Mg<sup>2+</sup>/Ca<sup>2+</sup> solvation analysis are available at [https://github.com/liuqilei/zhejiang\\_university](https://github.com/liuqilei/zhejiang_university).

### References

- Armand, M. & Tarascon, J. M. Building better batteries. *Nature* **451**, 652–657 (2008).
- Obama, B. The irreversible momentum of clean energy. *Science* **355**, aam6284 (2017).
- Cao, Y., Li, M., Lu, J., Liu, J. & Amine, K. Bridging the academic and industrial metrics for next-generation practical batteries. *Nat. Nanotechnol.* **14**, 200–207 (2019).
- Liang, Y., Dong, H., Aurbach, D. & Yao, Y. Current status and future directions of multivalent metal-ion batteries. *Nat. Energy* **5**, 646–656 (2020).
- Liang, Z. & Ban, C. Strategies to enable reversible magnesium electrochemistry: from electrolytes to artificial solid–electrolyte interphases. *Angew. Chem. Int. Ed.* **60**, 11036–11047 (2021).
- Wang, D. et al. Plating and stripping calcium in an organic electrolyte. *Nat. Mater.* **17**, 16–20 (2018).
- Hou, S. et al. Solvation sheath reorganization enables divalent metal batteries with fast interfacial charge transfer kinetics. *Science* **374**, 172–178 (2021).
- Dong, H. et al. High-power Mg batteries enabled by heterogeneous enolization redox chemistry and weakly coordinating electrolytes. *Nat. Energy* **5**, 1043–1050 (2020).
- Muldoon, J., Bucur, C. B. & Gregory, T. Fervent hype behind magnesium batteries: an open call to synthetic chemists—electrolytes and cathodes needed. *Angew. Chem. Int. Ed.* **56**, 12064–12084 (2017).
- Gummow, R. J., Vamvounis, G., Kannan, M. B. & He, Y. Calcium-ion batteries: current state-of-the-art and future perspectives. *Adv. Mater.* **30**, 1801702 (2018).
- Mohtadi, R., Tutusaus, O., Arthur, T. S., Zhao-Karger, Z. & Fichtner, M. The metamorphosis of rechargeable magnesium batteries. *Joule* **5**, 581–617 (2021).
- Attias, R., Salama, M., Hirsch, B., Goffer, Y. & Aurbach, D. Anode–electrolyte interfaces in secondary magnesium batteries. *Joule* **3**, 27–52 (2019).
- See, K. A. et al. The interplay of Al and Mg speciation in advanced Mg battery electrolyte solutions. *J. Am. Chem. Soc.* **138**, 328–337 (2016).
- Li, W. et al. Synthesis, crystal structure, and electrochemical properties of a simple magnesium electrolyte for magnesium/sulfur batteries. *Angew. Chem. Int. Ed.* **55**, 6406–6410 (2016).
- Xu, Y., Li, W., Zhou, G., Pan, Z. & Zhang, Y. A non-nucleophilic mono-Mg<sup>2+</sup> electrolyte for rechargeable Mg/S battery. *Energy Storage Mater.* **14**, 253–257 (2018).
- Wang, H. et al. Reversible electrochemical interface of mg metal and conventional electrolyte enabled by intermediate adsorption. *ACS Energy Lett.* **5**, 200–206 (2019).
- Li, Z. et al. Establishing a stable anode–electrolyte interface in Mg batteries by electrolyte additive. *ACS Appl. Mater. Interfaces* **13**, 33123–33132 (2021).
- Nguyen, D.-T. et al. A high-performance magnesium triflate-based electrolyte for rechargeable magnesium batteries. *Cell Rep. Phys. Sci.* **1**, 100265 (2020).
- Xiao, J. et al. Stable solid electrolyte interphase in situ formed on magnesium-metal anode by using a perfluorinated alkoxide-based all-magnesium salt electrolyte. *Adv. Mater.* **34**, e2203783 (2022).
- Muldoon, J. et al. Corrosion of magnesium electrolytes: chlorides—the culprit. *Energy Environ. Sci.* **6**, 482–487 (2013).
- Attias, R. et al. The role of surface adsorbed Cl<sup>−</sup> complexes in rechargeable magnesium batteries. *ACS Catal.* **10**, 7773–7784 (2020).
- Zhao-Karger, Z. et al. Toward highly reversible magnesium–sulfur batteries with efficient and practical Mg(B(hfp)<sub>4</sub>)<sub>2</sub> electrolyte. *ACS Energy Lett.* **3**, 2005–2013 (2018).
- Shyamsunder, A., Blanc, L. E., Assoud, A. & Nazar, L. F. Reversible calcium plating and stripping at room temperature using a borate salt. *ACS Energy Lett.* **4**, 2271–2276 (2019).
- Li, Z., Fuhr, O., Fichtner, M. & Zhao-Karger, Z. Towards stable and efficient electrolytes for room-temperature rechargeable calcium batteries. *Energy Environ. Sci.* **12**, 3496–3501 (2019).
- Tang, K. et al. A stable solid electrolyte interphase for magnesium metal anode evolved from a bulky anion lithium salt. *Adv. Mater.* **32**, e1904987 (2020).
- Ren, W. et al. An efficient bulky Mg(B(Otfe)<sub>4</sub>)<sub>2</sub> electrolyte and its derivatively general design strategy for rechargeable magnesium batteries. *ACS Energy Lett.* **6**, 3212–3220 (2021).
- Tutusaus, O. et al. An efficient halogen-free electrolyte for use in rechargeable magnesium batteries. *Angew. Chem. Int. Ed.* **54**, 7900–7904 (2015).
- Luo, J., Bi, Y., Zhang, L., Zhang, X. & Liu, T. L. A stable, non-corrosive perfluorinated pinacolatoborate Mg electrolyte for rechargeable Mg batteries. *Angew. Chem. Int. Ed.* **58**, 6967–6971 (2019).
- Zhao-Karger, Z., Gil Bardaji, M. E., Fuhr, O. & Fichtner, M. A new class of non-corrosive, highly efficient electrolytes for rechargeable magnesium batteries. *J. Mater. Chem. A* **5**, 10815–10820 (2017).
- Paskevicius, M. et al. Metal borohydrides and derivatives—synthesis, structure and properties. *Chem. Soc. Rev.* **46**, 1565–1634 (2017).
- Keyzer, Evan N. et al. A general synthetic methodology to access magnesium aluminate electrolyte systems for Mg batteries. *J. Mater. Chem. A* **7**, 2677–2685 (2019).
- Zhu, Y. et al. Effective synthesis of magnesium borohydride via B–O to B–H bond conversion. *Chem. Eng. J.* **432**, 134322 (2022).
- Hiyoshizo, K. et al. Facile reduction of benzenethiol ester under mild conditions with zinc borohydride. *Chem. Lett.* **15**, 1003–1004 (1986).

34. Forero-Saboya, J. et al. Understanding the nature of the passivation layer enabling reversible calcium plating. *Energy Environ. Sci.* **13**, 3423–3431 (2020).
35. Li, S. et al. Synergistic dual-additive electrolyte enables practical lithium-metal batteries. *Angew. Chem. Int. Ed.* **59**, 14935–14941 (2020).
36. Li, S. et al. High-efficacy and polymeric solid–electrolyte interphase for closely packed Li electrodeposition. *Adv. Sci.* **8**, 2003240 (2021).
37. Li, S. et al. Structured solid electrolyte interphase enable reversible Li electrodeposition in flame-retardant phosphate-based electrolyte. *Energy Storage Mater.* **42**, 628–635 (2021).
38. McClary, S. A. et al. A heterogeneous oxide enables reversible calcium electrodeposition for a calcium battery. *ACS Energy Lett.* **7**, 2792–2800 (2022).
39. Wang, X. et al. Glassy Li metal anode for high-performance rechargeable Li batteries. *Nat. Mater.* **19**, 1339–1345 (2020).
40. Son, S. B. et al. An artificial interphase enables reversible magnesium chemistry in carbonate electrolytes. *Nat. Chem.* **10**, 532–539 (2018).
41. Niu, C. et al. Self-smoothing anode for achieving high-energy lithium metal batteries under realistic conditions. *Nat. Nanotechnol.* **14**, 594–601 (2019).
42. Liu, J. et al. Pathways for practical high-energy long-cycling lithium metal batteries. *Nat. Energy* **4**, 180–186 (2019).
43. Fang, C. et al. Pressure-tailored lithium deposition and dissolution in lithium metal batteries. *Nat. Energy* **6**, 987–994 (2021).
44. Lu, T., Sobtop. Version 1.0 (dev3.1); <http://sobereva.com/soft/Sobtop>
45. Schauperl, M. et al. Non-bonded force field model with advanced restrained electrostatic potential charges (RESP2). *Commun. Chem.* **3**, 44 (2020).
46. Lu, T. & Chen, F. Multiwfn: a multifunctional wavefunction analyzer. *J. Comput. Chem.* **33**, 580–592 (2012).
47. Zhang, J. & Lu, T. Efficient evaluation of electrostatic potential with computerized optimized code. *Phys. Chem. Chem. Phys.* **23**, 20323–20328 (2021).
48. Becke, A. D. Density-functional thermochemistry. III. The role of exact exchange. *J. Chem. Phys.* **98**, 5648–5652 (1993).
49. Cancès, E., Mennucci, B. & Tomasi, J. A new integral equation formalism for the polarizable continuum model: theoretical background and applications to isotropic and anisotropic dielectrics. *J. Chem. Phys.* **107**, 3032–3041 (1997).
50. Miertus, S., Scrocco, E. & Tomasi, J. Electrostatic interaction of a solute with a continuum. A direct utilization of ab initio molecular potentials for the prevision of solvent effects. *Chem. Phys.* **55**, 117–129 (1981).
51. Hohenstein, E. G., Chill, S. T. & Sherrill, C. D. Assessment of the performance of the M05-2X and M06-2X exchange-correlation functionals for noncovalent interactions in biomolecules. *J. Chem. Theory Comput.* **4**, 1996–2000 (2008).
52. Marenich, A. V., Cramer, C. J. & Truhlar, D. G. Performance of SM6, SM8, and SMD on the SAMPL1 test set for the prediction of small-molecule solvation free energies. *J. Phys. Chem. B* **113**, 4538–4543 (2009).

## Acknowledgements

We owe our gratitude to Y. Yao and H. Dong for their help on this work. S.L. thanks his colleagues who still helped him complete this article after graduation. We thank L. Wu and S. Chang at the Center of Cryo-Electron Microscopy (CEM), Zhejiang University, for the technical assistance on Cryo-EM. We thank N. Zheng at State Key Laboratory of Chemical Engineering in Zhejiang University for performing SEM and Raman. We thank Y. Lu at the school of Materials Science and Engineering in Zhejiang University for performing XPS. We thank D. Chen from Shiyanjia Lab ([www.shiyanjia.com](http://www.shiyanjia.com)) for providing invaluable assistance with the X-ray single-crystal analysis. We acknowledge financial support from the Natural Science Foundation of China (22022813, 21878268), the National Key R&D Program of China (2018YFA0209600), the Leading Innovative and Entrepreneur Team Introduction Program of Zhejiang (2019R01006), the Key R&D Program of Zhejiang Province (2019C01155) and the Fundamental Research Funds for China Central Universities (DUT22LAB608).

## Author contributions

S.L. conceived the idea and designed the experiments. S.L. and J.Z. synthesized the electrolytes. Q.L. and H.C. performed the DFT/MD calculation. S.Z. provided the PVA separator. H.C. and X.W. synthesized and fabricated sulfur electrodes. L.F., W.Z. and Q.W. prepared GO/Cu membranes. All authors participated in writing the manuscript. Y.L. supervised the project.

## Competing interests

S.L., H.C., J.Z., S.Z. and Y.L. declare that this work has been filed as Chinese Patent Application number 2023102361925. All other authors declare no competing interests.

## Additional information

**Supplementary information** The online version contains supplementary material available at <https://doi.org/10.1038/s41560-023-01439-w>.

**Correspondence and requests for materials** should be addressed to Yingying Lu.

**Peer review information** *Nature Energy* thanks Toshihiko Mandai and the other, anonymous, reviewer(s) for their contribution to the peer review of this work.

**Reprints and permissions information** is available at [www.nature.com/reprints](http://www.nature.com/reprints).

**Publisher's note** Springer Nature remains neutral with regard to jurisdictional claims in published maps and institutional affiliations.

Springer Nature or its licensor (e.g. a society or other partner) holds exclusive rights to this article under a publishing agreement with the author(s) or other rightsholder(s); author self-archiving of the accepted manuscript version of this article is solely governed by the terms of such publishing agreement and applicable law.

© The Author(s), under exclusive licence to Springer Nature Limited 2024